

## The effects of strain on the ordered phases of $\text{Ni}_x\text{Pt}_{1-x}$ ( $x=0.25, 0.5, \text{ and } 0.75$ )

I. G. Shuttleworth,  
School of Science and Technology,  
Nottingham Trent University,  
Nottingham NG11 8NS.  
UK

E-mail: [ian.shuttleworth@ntu.ac.uk](mailto:ian.shuttleworth@ntu.ac.uk)

### Abstract

The effects of strain on the ordered  $L1_0$  and  $L1_2$  phases of  $\text{Pt}_x\text{Ni}_{1-x}$  ( $x=0.25, 0.5, \text{ and } 0.75$ ) have been investigated using both scalar and vector relativistic density functional theory (DFT). The spin orbit correction (SOC) orders the local magnetic moment vector along  $\Gamma R$  ( $\Gamma A$ ) diagonal of the  $L1_2$  ( $L1_0$ ) phases. Applying tensile (compressive) strain to each phase causes the local magnetic moment of the crystal to increase (decrease). The SOC component of the local magnetic moment is independent of the stress applied to the crystal.

## 1. Introduction

Transition metal alloys have been widely seen to form solid solutions which develop magnetically under the influence of composition, temperature, and pressure. A series of subtle interactions control this behaviour, and the nature of these interactions is a subject of current interest. Structurally [1] these materials can appear as substitutionally disordered phases, or as an ordered phase, and can undergo a transition between structural phases with changes in temperature, pressure or stoichiometry. The magnetic character of the system can also be seen to undergo a phase transition during changes in these parameters and can either proceed alongside a structural phase transition or in lieu of structural change.

The Pt-based bimetallic alloys are chemically ordered below an order-disorder transition temperature. The ordered Ni-Pt [2-3] and Co-Pt [4] alloys have either an  $L1_0$  (P4/mmm) structure (CuAu type) or an  $L1_2$  ( $Pm\bar{3}m$ ) structure (Cu<sub>3</sub>Au type) depending on the stoichiometry. These ordered systems disorder above order-disorder transition temperature; in the disordered system, the components of the alloy are randomly distributed on FCC lattice sites. Thermal hysteresis of 50K has been observed around an order-disorder transition temperature of 913K [5] with the  $L1_2$  structure tending to demonstrate a higher degree of chemical ordering.

The local magnetic moment of the Ni atoms are sensitive to the concentration within the alloy and to the presence of local order. Estimates of the moment are further sensitive to the type of estimation performed – density functional theory (DFT) estimates of the Ni magnetic moment [6, 7-8] lie in the region of approximately 0.2-0.6 $\mu_B$  whereas the Pt moment lies in the region of approximately 0.1-0.2/0.3 $\mu_B$ . The variance in these quantities is predominantly due to the concentration of Ni and Pt. For simulations of the Ni<sub>3</sub>Pt  $L1_2$  structure the larger values of the Ni moment are seen, approaching the pure Ni value of 0.616 $\mu_B$  [7]. The Ni moment becomes progressively smaller as the Ni concentration becomes less and the NiPt  $L1_0$  and the Ni<sub>3</sub>Pt  $L1_2$  structures are simulated. A second source of variance is the type of functional used with LDA estimates of the exchange-correlation tending to estimate moments that are approximately 0.1 $\mu_B$  lower than the corresponding GGA estimates. GGA estimates of the local magnetic moment are seen to be closer to the experimental values than their LDA counterparts [6] with relativistic terms [7] improving the agreement. For these reasons the GGA is used exclusively in the current work.

So far, only the behaviour of the unstrained alloy has been considered. However, the importance of strain engineering with metallic systems is becoming widely recognised; in these investigations, the system is loaded with either tensile or compressive strains in order to effect changes in the nature of the system. Mechanisms to effect strain particularly on surfaces are developing, and one mechanism is used when pure metal layers form on alloy surfaces. In these circumstances, the lattice mismatch between the metal and alloy produces either a compressive or a tensile force in the surface layer. A widely recognised example of this is Pt<sub>3</sub>Ni(111) [9-11] which is 10-times more active in the oxygen reduction reaction (ORR) than Pt(111). Pure Pt overlayers form on this surface and over a series of similarly low Miller index surfaces [12-

14]. The formation of these overlayers is not unique to Pt-Ni alloys and are seen across a range of bimetallic alloy surfaces [15].

However, the mechanism by which the surface reactivity changes for phase separated alloys is not clearly understood. Recent studies of the ideally bulk-terminated and Pt-terminated Pt<sub>3</sub>Ni surfaces [16] have discussed changes in the magnetic character of atoms and the electronic structure at the surface. More recent studies have investigated the effect of strain on the binding of hydrogen on pure Pt [17] and across a large range of pure, un-alloyed transition metal surfaces [18]. The results have shown that as the for strains of up to 2% surface adsorbed H undergoes a structural transformation on Pt [17], Pd and Ir [18] surfaces, and similarly undergoes structural transformations on other Fe, Rh, Ag and Os surfaces for larger strains [18]. The electronic state of the H atoms in these systems undergo significant changes during these structural transformations; this state is clearly then tuneable and directly involved in the reactivity of the surface particularly during H-bearing reactions such as the ORR.

A satisfactory understanding of the strained and unstrained bulk Pt-Ni alloy is a necessary precursor to studies of the surfaces. In addition, strain engineering of bulk magnets is a useful probe of the magnetic character of the system. Magnetism arises because of competition between the exchange mechanisms within the crystal and the motion of atoms. Deliberately deforming the crystal will cause the system to respond in a way that is controlled by and symptomatic of these mechanisms. Studies of the effect of volume changes on bcc Ni, fcc Co, bcc V and fcc Fe [19] have shown that non-magnetic/magnetic phase transitions occur in these systems and that the local magnetic moment curve may be simply modelled using a Landau energy expansion. Complementary experimental studies of both the pure [20] and hydrogenated [21] Fe, Ni and Co systems have explored the behaviour of the ferromagnetic state under pressure and have identified a distinct structural dependence of the state as well as its mediation by hydrogenation. Studies of the CeNi<sub>5</sub> system [22] have used the Crystal Orbital Overlap Population (COOP) to develop an understanding of the mechanisms controlling the system response to strain as well as determining the response itself. Using this analysis it was shown that the Ce 4f and Ni 3d states carry the magnetic moment of the system and that Ce 4f moment is relatively insensitive to strain compared to the response of the Ni 3d moment. The study also showed that a significant strain-dependent interaction exists between Ce 6s–Ni 4s states which are delocalised and non-magnetic in character, and a weaker set of interactions exist indicating competition localised and delocalised mechanisms exist in the crystal.

The current work will investigate the local magnetic moment of the bulk Pt<sub>3</sub>Ni, PtNi and PtNi<sub>3</sub> phases using both scalar and vector relativistic density functional theory (DFT) and will, in part, clarify the role played by the spin-orbit correction (SOC) when the crystals are in equilibrium (zero strain) and when the crystals are subject to both compressive and tensile strain. The work is structured in the following way: in section 2 the Computational Details are presented, then in section 3 the computational results for each phase are presented and discussed in turn. Section 4 will then summarise and discuss the main findings of the work.

## 2. Computational Details

The plane-wave density functional theory (DFT) simulations presented in this work were performed using the Quantum Espresso package [23]. Brillouin zone sampling was performed using a first-order Methfessel-Paxton smearing of 0.02 Ry [24]. Scalar and vector relativistic ultra-soft pseudopotentials with non-linear core corrections were used [25-26] together wave-function kinetic energy cut-off of 75 Ry and a charge density/potential kinetic energy cut-off of 900 Ry. Both collinear and non-collinear spin-polarised simulations were performed in the current work. Vector (scalar) relativistic pseudopotentials were used exclusively for the non-collinear (collinear) simulations. In order to ensure that the magnetic lowest energy state was determined during the self-consistent cycle of the non-collinear simulations the polar and azimuthal angles were stepped in increments of  $\pi/4$  through ranges of  $[0, 2\pi]$  for each non-collinear simulation and the simulation was restarted for each initial orientation.

Fig. 1 shows the structural models for the  $\text{Pt}_3\text{Ni}$ ,  $\text{PtNi}_3$  and  $\text{PtNi}$  systems. Table 1 summarises the structural parameters determined for these systems. To ensure convergence, the determined structural parameters presented in Table 1 were compared with parameters obtained from simulations using a wave-function kinetic energy cut-off and a charge density/potential kinetic energy cut-off of 100 Ry and 1200 Ry, respectively, and no significant difference was noticed. The results in Table 1 indicate that the structural parameters are significantly improved when compared to the experimental values by the inclusion of semi-core states and this improvement generally continued with the inclusion of an f semi-core state to the Pt pseudopotential. The Brillouin zone sampling was performed on a sequence of  $(6 \times 6 \times 6)$ ,  $(8 \times 8 \times 8)$ ,  $(10 \times 10 \times 10)$ ,  $(12 \times 12 \times 12)$ ,  $(14 \times 14 \times 14)$ ,  $(16 \times 16 \times 16)$ ,  $(18 \times 18 \times 18)$ , and  $(20 \times 20 \times 20)$  grids. Convergence was identified with a sampling between  $(12 \times 12 \times 12)$  and  $(14 \times 14 \times 14)$ . A Brillouin zone sampling of  $(20 \times 20 \times 20)$  was used for all the results presented in this work.

Lattice strain  $\varepsilon$  was defined as

$$\varepsilon = \left( \frac{a_s - a}{a} \right) \times 100\% \quad (1)$$

The strained and equilibrium (zero strain) lattice constants are  $a_s$  and  $a$ , respectively. The range of  $\varepsilon$  was  $\pm 5\%$  was decided to be comparable with the lattice mismatch between the Pt-Ni alloys and pure Pt and Ni metals. For the  $L1_0$  simulations the ratio  $c/a$  was not changed during strain; consequently, the strained and equilibrium [001] lattice constants,  $c_s$  and  $c$  respectively, were related by

$$\frac{c_s}{a_s} = \frac{c}{a} \quad (2)$$

### 3. Results and Discussion

Fig. 2 shows the local magnetic moment  $\mu$  of each of the Pt d and Ni d states in the Pt<sub>3</sub>Ni, PtNi and PtNi<sub>3</sub> alloys under strain  $\epsilon$ . The local magnetic moment of each of the Pt and Ni d states increases with  $\epsilon$  and are ferromagnetically ordered at  $\epsilon=0$ . These increases are approximately linear for the L<sub>12</sub> phases and for the tensile ( $\epsilon>0$ ) L<sub>10</sub> phases; for the compressively strained L<sub>10</sub> the increases are non-linear. The local magnetic moment was evaluated for both non-collinear and collinear spin polarisation. The curvatures of the two sets of curves are seen to be very similar. The most significant difference between the non-collinear and collinear simulations are that the curves are offset from one another suggesting that the most significant difference between the two sets of simulations is a local magnetic moment which remains constant under strain.

The local magnetic moment was seen to only exist in the Pt and Ni d states for all  $\epsilon$ . To investigate the mechanism which drives these changes a population analysis of all of the Ni and Pt states was performed. This analysis will be summarised now though is presented in full in the Supplementary Table S1. The fractional change in the occupation of each of the Pt and Ni s, p and d states are 0.2-0.5% under strain. These fractional changes were seen to be comparable for simulations which used Pt (spf) Ni (sp) and Pt (sp) Ni (sp) semi-core states, when compared with simulations that did not use semi-core states. Consequently, because the Pt (spf) simulations required more computation time but did not yield significantly more precise results compare to the Pt (sp) simulations, all subsequent calculations were performed using pseudopotentials that have Pt (sp) Ni (sp) semi-core states.

The fractional changes in the occupation of each of the Pt and Ni s, p and d states during strain are insufficient to explain the changes in local magnetic moment seen in Fig. 2. Consequently transitions between d sub-orbitals must be responsible. This assertion is quantified in Fig. 3 for the non-collinear case. Fig. 3 shows the variance  $v$  in the occupation of the of the non-collinear  $m_j$  components Ni and Pt d states for each of the alloys under strain  $\epsilon$ . As the variance increases then the differences in occupations of the non-collinear  $m_j$  components changes which results in a magnetic moment. The variances are greatest for the Ni d states which is consistent with Fig. 2 which shows that the greater magnetic moment is carried by the Ni d states compared to the Pt d states.

Fig. 4 shows the band structures of the Pt<sub>3</sub>Ni, PtNi and PtNi<sub>3</sub> alloys under equilibrium ( $\epsilon=0\%$ ) and under the extremes of strain considered in the current work ( $\epsilon=\pm 5\%$ ). The band structures were calculated using non-collinear spin polarisation. For each alloy the band structures show a narrowing as the strain becomes increasing tensile and markedly a sequence of horizontal states in the  $\Gamma$ R [29] interval of the L<sub>12</sub> dispersions, the XM interval of the PtNi<sub>3</sub> dispersion and around the  $\Gamma$  point in the L<sub>10</sub> dispersion.

The total spin polarisation  $S(\mathbf{k}, E)$  was defined as

$$S(\mathbf{k}, E) = \sqrt{S_1^2(\mathbf{k}, E) + S_2^2(\mathbf{k}, E) + S_3^2(\mathbf{k}, E)} \quad (3)$$

$S_1$ ,  $S_2$ , and  $S_3$  are the expectation values of the  $\sigma_1$ ,  $\sigma_2$  and  $\sigma_3$  Pauli spin operators, respectively.  $S_k(k)$  was defined by

$$S_k(k) = \int_{E=-\infty}^{E_F} S(k, E) dE \quad (4)$$

The  $S_k(k)$  are shown in Fig. 4. It can be seen that the  $S_k(k)$  are dispersed throughout k-space, both along components which lie in the  $\{001\}$  portions of the space and those that lie along the diagonal  $\Gamma R$  sections. Considering the components of  $S_k(k)$ , the  $S_1$  and  $S_2$  were generally zero and  $S_k(k)$  was defined by  $S_3$ . The  $S_1$  and  $S_2$  were non-zero along the  $\Gamma R$  diagonal of all alloys and along the  $\Gamma A$  diagonal of the  $L1_0$  PtNi phase. Additional regions satisfying  $S_1=0$  and  $S_2 \neq 0$  along the  $XA$  direction and  $S_1 \neq 0$  and  $S_2=0$  along the  $\Gamma A$  direction of the  $L1_0$  PtNi alloy.

It has already been shown that the variation in magnetism under strain is predominantly independent of whether spin-orbit corrected (vector relativistic) non-collinear spin polarisation or scalar relativistic collinear simulations should be used. Consequently the directional component observed in the band structure analysis may be anticipated to have little effect on the local magnetic moment. However the effect of strain on the directional component cannot be inferred from this observation. So, to investigate the stability of these directional components under strain Fig. 5 shows the correlation between the  $S_1$  for alloys under strains of  $\epsilon = \pm 5\%$  with the alloy at equilibrium ( $\epsilon = 0\%$ ). Each panel in Fig. 5 shows a black line with unit gradient. If  $S_1$  is entirely unaffected by  $\epsilon$  then the data in panel will lie along this line. The deviation of the data from this line is a measure of the effect of  $\epsilon$  on  $S_1$ . The red line is a best fit straight line through the data of each panel. It can be seen that, for the  $L1_2$  alloys, when the ordinate is  $S_1|_{\epsilon=-5\%}$  ( $S_1|_{\epsilon=+5\%}$ ) that the slope of the red line is greater than (less than) zero. This shows that, very generally, the magnitude of  $S_1$  increases (decreases) under compressive (tensile) for the  $L1_2$  alloys. The situation is more complicated for the  $L1_0$  PtNi alloy where the correlation between strained and unstrained  $S_1$  is lower than for the  $L1_2$  alloys and consequently the linear analysis is less likely to be a reliable metric.

#### 4. Conclusions

The current work has investigated the local magnetic moment of the ordered  $L1_0$  and  $L1_2$  phases of  $Pt_3Ni$ ,  $PtNi$  and  $PtNi_3$  using both scalar and vector relativistic density functional theory (DFT). The scalar and vector relativistic simulations were performed using collinear and non-collinear spin, respectively. The effect of straining each alloy is to decrease or increase the magnetism of the alloy depending whether the strain is either compressive or tensile, respectively. Analysing the charge populations of each alloy when strain is applied shows that the Ni and Pt d orbitals are magnetised whereas all the other orbitals are non-magnetic. For non-collinear simulations, the change in local magnetic moment is accompanied by charge

transfer between sub-shells of  $m_j$ . However, the total occupation of each total angular momentum  $j$  subshell remains constant.

Comparing the band structures of each alloy under strain ( $\epsilon=\pm 5\%$ ) and at equilibrium ( $\epsilon=0\%$ ) shows that the band structures become narrower as the strain becomes increasingly tensile. The vector-relativistic non-collinear simulations have shown that a directional component of local magnetic moment lies along the  $\Gamma R$  and  $\Gamma A$  diagonals of the  $L_{12}$  and  $L_{10}$  phases, respectively. This directionality doesn't significantly affect the behaviour of the local magnetic moment of the entire unit cell under strain but the magnitude of the directional component is affected by strain.

## Acknowledgements

This work was supported by the computational resources of the Supercomputing Laboratory at the King Abdullah University of Science & Technology (KAUST) and by the author's membership of the UK's HEC Materials Chemistry Consortium, which is funded by the EPSRC (**EP/L000202**) and used the ARCHER UK National Supercomputing Service (<http://www.archer.ac.uk>).

## References

- [1] M. C. Cadeville, and J. L. Morán-López. Magnetism and spatial order in transition metal alloys: Experimental and theoretical aspects. *Phys. Repts.* **153(6)** (1987) 331-399.
- [2] C. E. Dahmani, M. C. Cadeville, J. M. Sanchez, and J. L. Morn-Lpez. Ni-Pt phase diagram: Experiment and theory. *Phys. Rev. Lett.* **55(11)** (1985) 1208-1211.
- [3] H. Okamoto. Ni-Pt (Nickel-Platinum). *J Phase Equilibria Diffus.* **31(3)** (2010) 322-322.
- [4] Y. Le Bouar, A. Loiseau, and A. Finel. Origin of the complex wetting behavior in Co-Pt alloys. *Phys. Rev. B: Condens. Matter* **68(22)** (2003) 224203.
- [5] O. Seo, J. Y. Lee, J. M. Kim, J.-W. Kim, H. C. Kang, J. Chung, and D. Y. Noh. Chemical ordering in PtNi nanocrystals. *J. Alloys Compd.* **666** (2016) 232-236.
- [6] U. Kumar, P. K. Mukhopadhyay, B. Sanyal, O. Eriksson, P. Nordblad, D. Paudyal, K. Tarafder, and A. Mookerjee. Experimental and theoretical study of annealed Ni-Pt alloys. *Phys. Rev. B: Condens. Matter* **74(6)** (2006) 064401.

- [7] P. P. Singh. Relativity and magnetism in Ni-Pd and Ni-Pt alloys. *J. Magn. Magn. Mater.* **261** (2003) 347-352.
- [8] D. Paudyal, T. Saha-Dasgupta, and A. Mookerjee. Magnetic properties of X-Pt (X = Fe, Co, Ni) alloy systems. *J. Phys.: Condens. Matter* **16** (2004) 2317-2334.
- [9] V. R. Stamenkovic, B. Fowler, B. S. Mun, G. Wang, P. N. Ross, C. A. Lucas, and N. M. Marković; Improved Oxygen Reduction Activity on Pt<sub>3</sub>Ni(111) via Increased Surface Site Availability. *Science* **315** (2007) 493-497.
- [10] V. R. Stamenkovic, B. S. Mun, M. Arenz, K. J. J. Mayrhofer, C. A. Lucas, G. Wang, P. N. Ross, and N. M. Marković. Trends in electrocatalysis on extended and nanoscale Pt-bimetallic alloy surfaces. *Nature Mater.* **6(3)** (2007) 241-247.
- [11] Y. Nie, L. Li, and Z. Wei. Recent advancements in Pt and Pt-free catalysts for oxygen reduction reaction. *Chem. Soc. Rev.* **44** (2015) 2168-2201.
- [12] B. S. Mun, M. Watanabe, M. Rossi, V. Stamenkovic, N. M. Markovic, and P. N. Ross. The study of surface segregation, structure and valence band density of states of Pt<sub>3</sub>Ni(100), (110), and (111) crystals. *Surf. Rev. Lett.* **13(5)** (2006) 697-702.
- [13] Y. Ma, and P. B. Balbuena. Pt surface segregation in bimetallic Pt<sub>3</sub>M alloys: A density functional theory study. *Surf. Sci.* **602** (2008) 107-113.
- [14] W. Hebenstreit, G. Ritz, M. Schmid, A. Biedermann, and P. Varga. Segregation and reconstructions of Pt<sub>x</sub>Ni<sub>1-x</sub>(100). *Surf. Sci.* **388** (1997) 150-161.
- [15] M. Polak, and L. Rubinovich. The interplay of surface segregation and atomic order in alloys. *Surf. Sci. Repts.* **38** (2000) 127-194.
- [16] B. K. Sharma, O. Kwon, D. Odkhuu, and S. C. Hong. Electronic structure and magnetism of various surfaces of the catalytic material Pt<sub>3</sub>Ni: Density-functional study. *J. Magn. Magn. Mater.* **339** (2013) 89-93.
- [17] I. G. Shuttleworth, Controlled FCC/on-top binding of H/Pt(111) using surface stress. *App. Surf. Sci.* **378** (2016) 286-292.

- [18] I. G. Shuttleworth, Strain engineering of H/transition metal systems. *Surf. Sci.* **661** (2017) 49-59.
- [19] V. L. Moruzzi. Singular Volume Dependence of Transition-Metal Magnetism. *Phys. Rev. Lett.* **57(17)** (1986) 2211-2214.
- [20] N. Ishimatsu, H. Maruyama, N. Kawamura, M. Suzuki, Y. Ohishi, and O. Shimomura. Stability of ferromagnetism in Fe, Co, and Ni metals under high pressure. *J. Phys. Soc. Jpn.* **76(6)** (2007) 064703.
- [21] N. Ishimatsu, T. Shichijo, Y. Matsushima, H. Maruyama, Y. Matsuura, T. Tsumuraya, T. Shishidou, T. Oguchi, N. Kawamura, M. Mizumaki, T. Matsuoka, and K. Takemura. Hydrogen-induced modification of the electronic structure and magnetic states in Fe, Co, and Ni monohydrides. *Phys. Rev. B: Condens. Matter* **86(10)** (2012) 104430
- [22] I. G. Shuttleworth. Strain Engineering of the CeNi<sub>5</sub> System. *Magnetochemistry* **2(4)** (2016) 39-1/12.
- [23] P. Giannozzi, S. Baroni, N. Bonini, M. Calandra, R. Car, C. Cavazzoni, D. Ceresoli, G. L. Chiarotti, M. Cococcioni, I. Dabo, A. Dal Corso, S. Fabris, G. Fratesi, S. de Gironcoli, R. Gebauer, U. Gerstmann, C. Gougoussis, A. Kokalj, M. Lazzeri, L. Martin-Samos, N. Marzari, F. Mauri, R. Mazzarello, S. Paolini, A. Pasquarello, L. Paulatto, C. Sbraccia, S. Scandolo, G. Sclauzero, A.P. Seitsonen, A. Smogunov, P. Umari, and R. M. Wentzcovitch. QUANTUM ESPRESSO: a modular and open-source software project for quantum simulations of materials. *J. Phys.: Condens. Matter.* **21** (2009) 395502.
- [24] M. Methfessel, and A.T. Paxton. High-precision sampling for Brillouin-zone integration in metals. *Phys. Rev. B: Condens. Matter* **40** (1989) 3616–3621.
- [25] The x.pbe-n-rrkjus\_psl.1.0.0.UPF, x.pbe-spn-rrkjus\_psl.1.0.0.UPF, Pt.pbe-spf-n-rrkjus\_psl.1.0.0.UPF, x.rel-pbe-n-rrkjus\_psl.1.0.0.UPF, x.rel-pbe-spn-rrkjus\_psl.1.0.0.UPF, and Pt.rel-pbe-spf-n-rrkjus\_psl.1.0.0.UPF, where x=Pt or Ni, pseudopotentials were used from the Quantum ESPRESSO pseudopotential data base: <http://www.quantum-espresso.org/pseudopotentials>.

- [26] A. Dal Corso. Pseudopotentials periodic table: From H to Pu. *Comput. Mater. Sci.* **95** (2014) 337-350.
- [27] A. Pisanty, C. Amador, Y. Ruiz, and M. de la Vega. Band structures of Ni<sub>3</sub>Pt and NiPt<sub>3</sub>. *Z. Phys. B – Condens. Matter* **80** (1990) 237-239.
- [28] W. B. Pearson. *A Handbook of Lattice Spacings and Structures of Metals and Alloys*. (Pergamon Press, Oxford, 1967).
- [29] W. Setyawan, and S. Curtarolo. High-throughput electronic band structure calculations: Challenges and tools. *Comput. Mater. Sci.* **49(2)** (2010) 299-312.

Table 1. Summary of the structural parameters of the Pt<sub>3</sub>Ni (L1<sub>2</sub>), PtNi (L1<sub>0</sub>) and PtNi<sub>3</sub> (L1<sub>2</sub>) systems. The results in these tables were determined under equilibrium conditions where the strain was zero, and for both scalar- and vector-relativistic pseudopotentials. C denotes collinear (scalar relativistic) and NC non-collinear (vector relativistic).

Structure	Pseudopotential semi-core states	a (Å)			c (Å)		
		C	NC	Exptl	C	NC	Exptl
PtNi	-	3.854	3.854	3.814[27]	3.634	3.627	3.533[28]
	Pt (sp) Ni (sp)	3.830	3.831		3.616	3.586	
	Pt (spf) Ni (sp)	3.824	3.824		3.614	3.579	
Pt <sub>3</sub> Ni	-	3.886	3.887	3.836[27]			
	Pt (sp) Ni (sp)	3.869	3.868				
	Pt (spf) Ni (sp)	3.860	3.860				
PtNi <sub>3</sub>	-	3.660	3.660	3.645[27]			
	Pt (sp) Ni (sp)	3.634	3.634				
	Pt (spf) Ni (sp)	3.630	3.630				

Fig. 1. Models of the (a-b)  $\text{Pt}_3\text{Ni}$  ( $L1_2$ ) and (c-d)  $\text{PtNi}$  ( $L1_0$ ) unit cells. In both sets of figures the large white/light grey (small dark grey) circles denote Pt (Ni) atoms. In (a-b) the large grey circles are Pt atoms which are co-planar in (001) with Ni atoms whereas the large white circles are Pt atoms which are shifted by half a lattice spacing from the Ni atoms along the [001] direction. The  $\text{PtNi}_3$  unit cell is obtained by replacing each Pt (Ni) atom with Ni (Pt) in the  $\text{Pt}_3\text{Ni}$ .

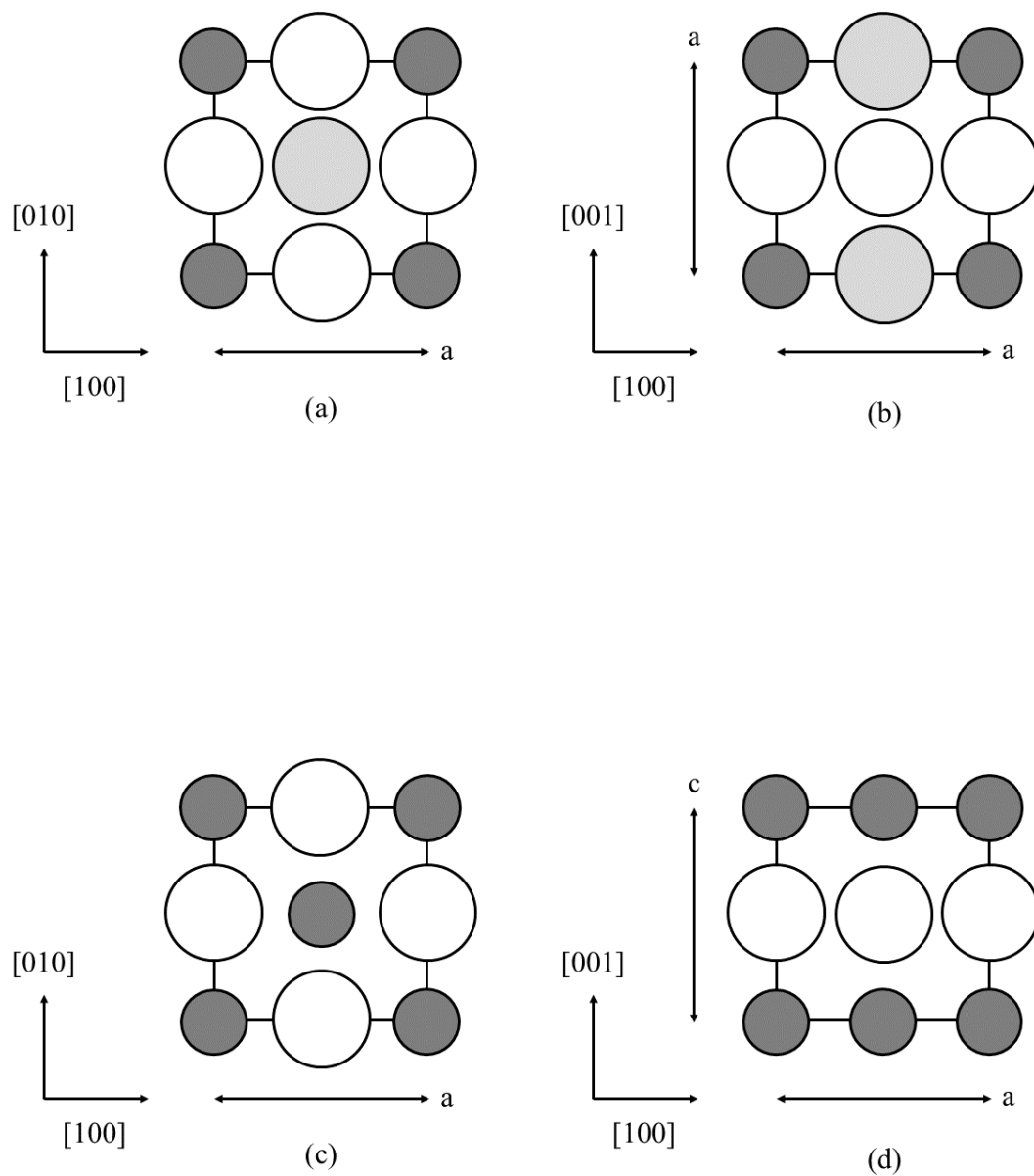


Fig. 2. Local magnetic moment  $\mu$  of the (a) Ni d, and (b) Pt d states, versus strain  $\epsilon$  for each of the Pt<sub>3</sub>Ni, PtNi and PtNi<sub>3</sub> alloys, The black (grey) lines are from non-collinear (collinear) simulations.

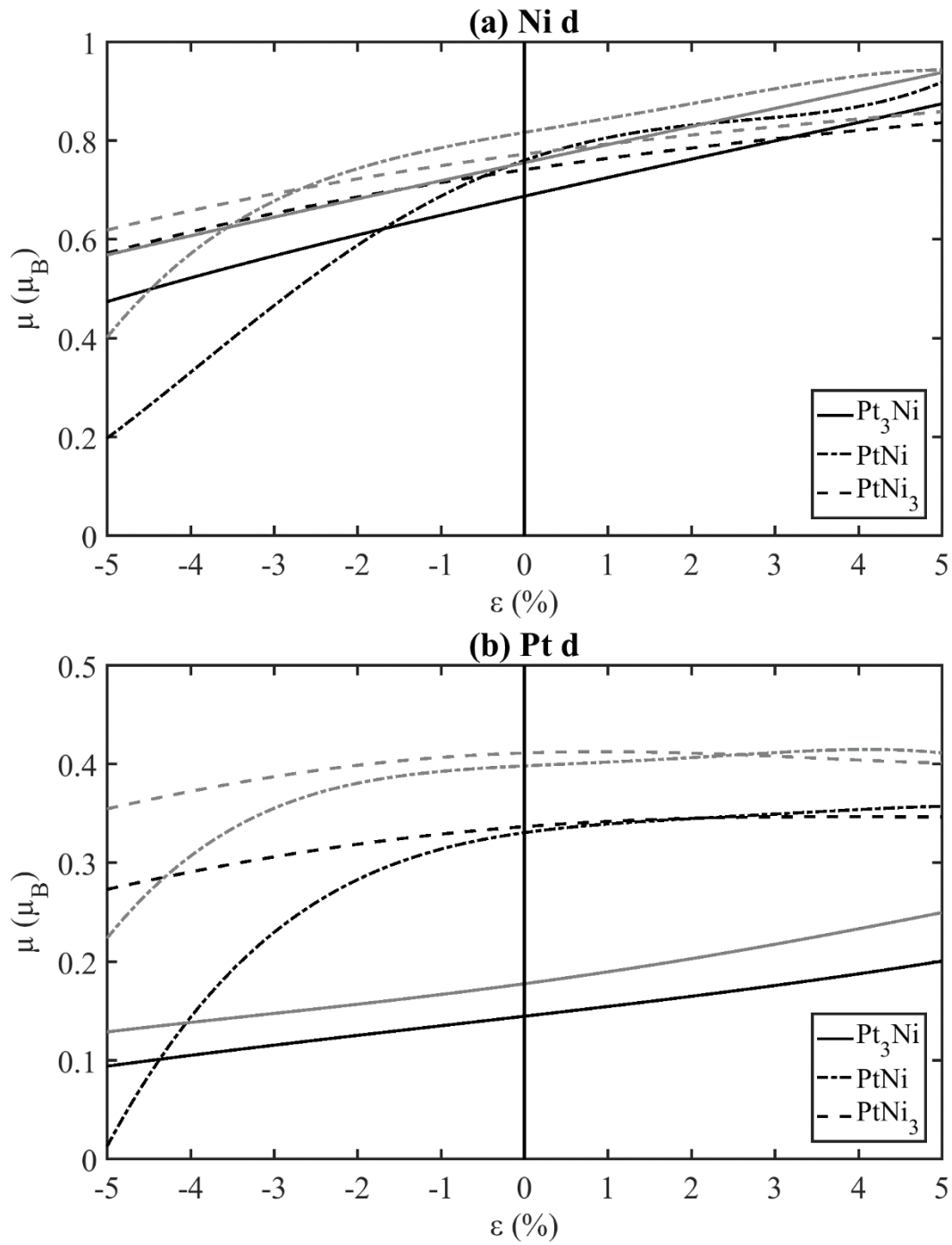


Fig. 3. Variance  $v$  in the occupation of the of the non-collinear  $m_j$  components Ni and Pt d states for the (a)  $\text{Pt}_3\text{Ni}$ , (b)  $\text{PtNi}$ , and (c)  $\text{PtNi}_3$  alloys under strain  $\varepsilon$ .

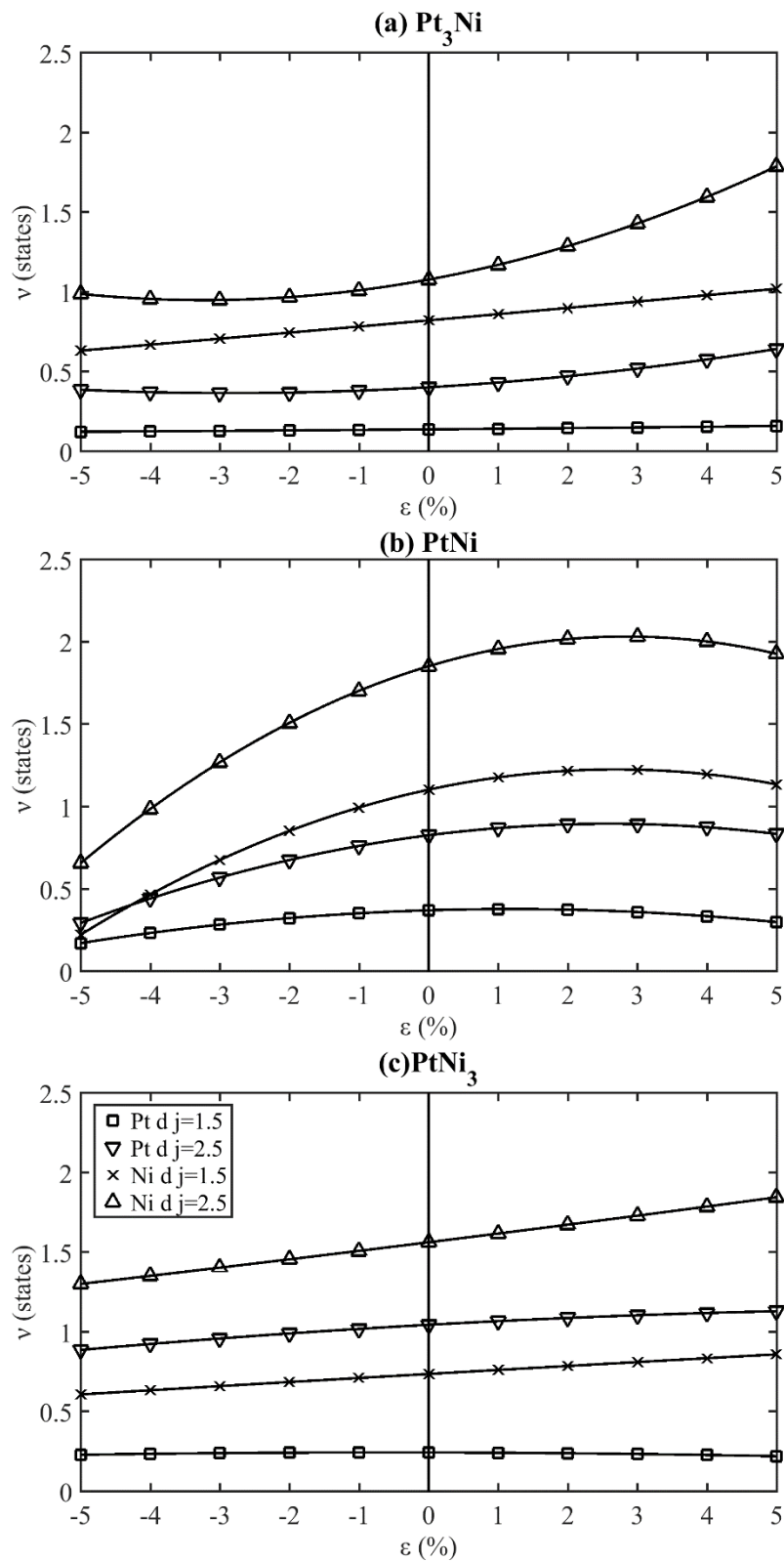
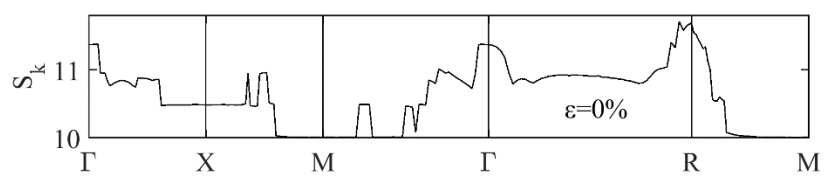
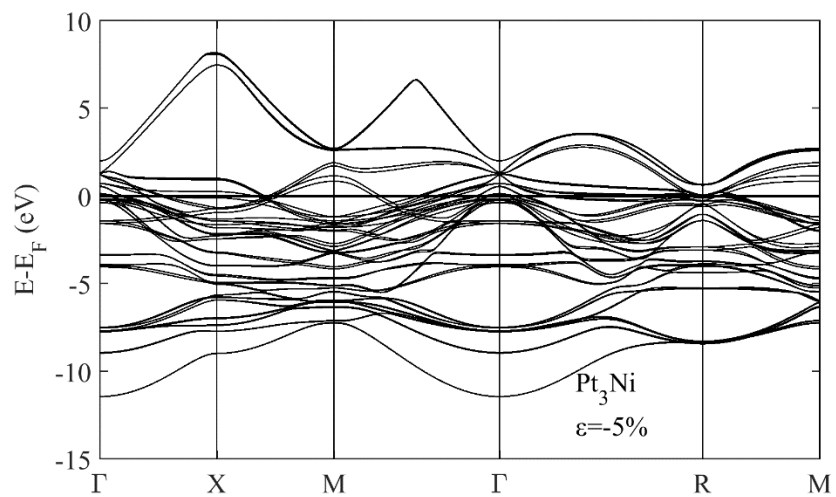
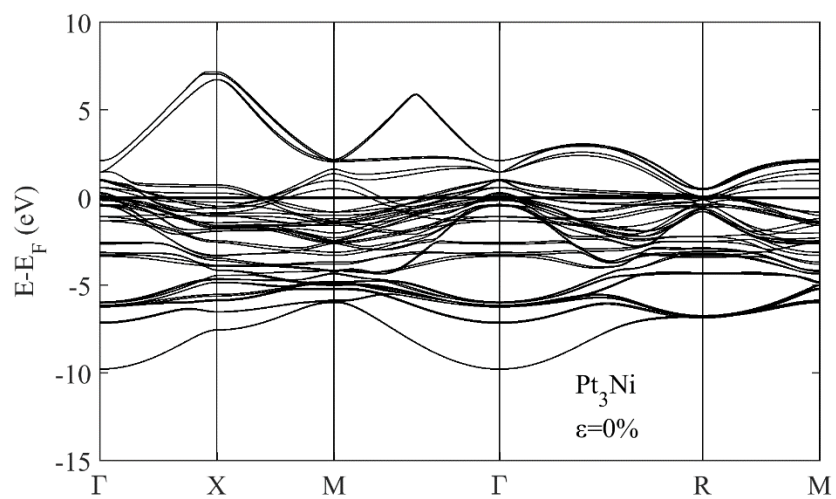
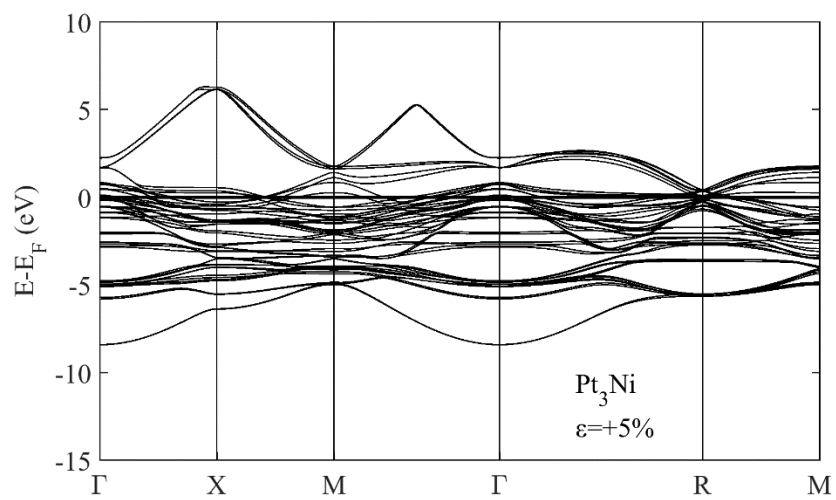
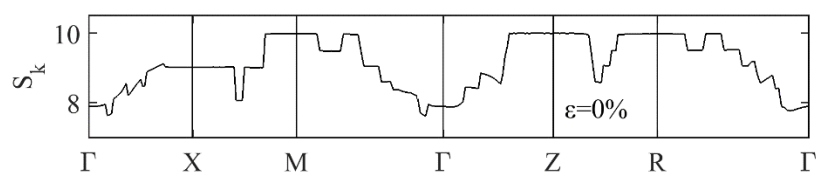
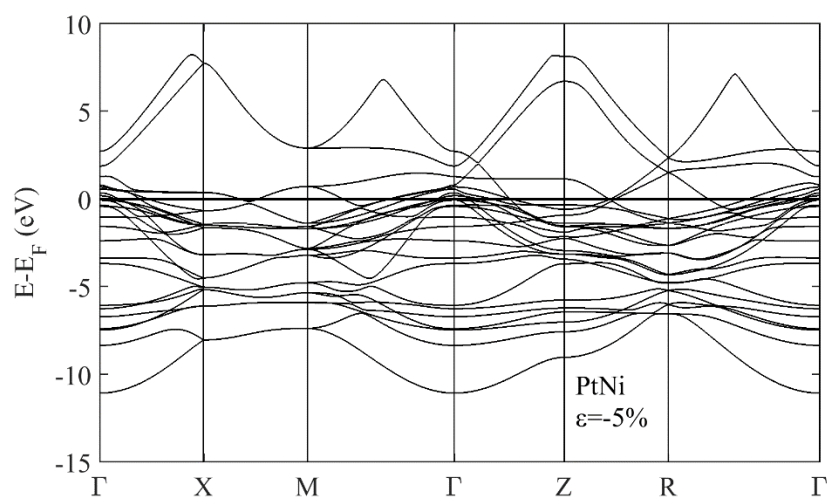
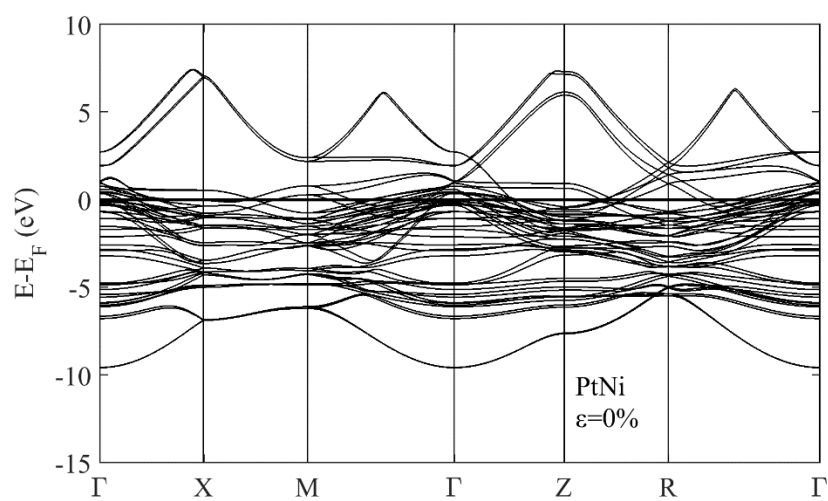
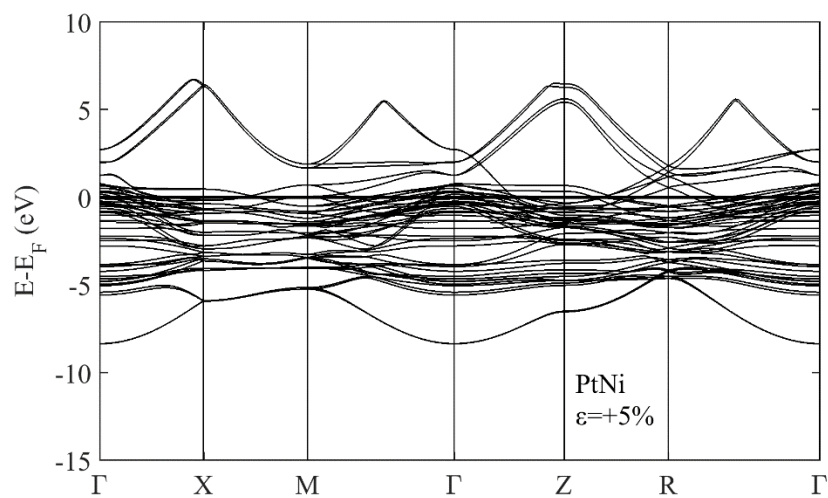


Fig. 4. Band structure and the  $k$ -resolved total spin polarisation  $S_k$  for the (a)  $\text{Pt}_3\text{Ni}$ , (b)  $\text{PtNi}$ , and (c)  $\text{PtNi}_3$  alloys under tensile ( $\varepsilon=+5\%$ ), zero ( $\varepsilon=0\%$ ), and compressive ( $\varepsilon=-5\%$ ) strain.

(a)



(b)



(c)

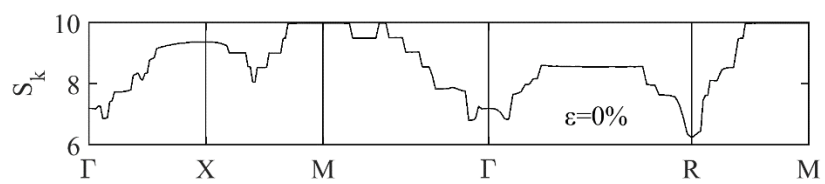
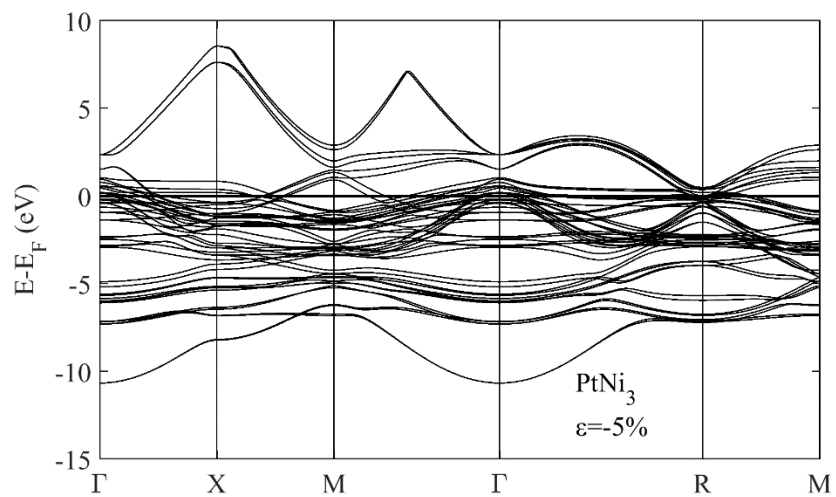
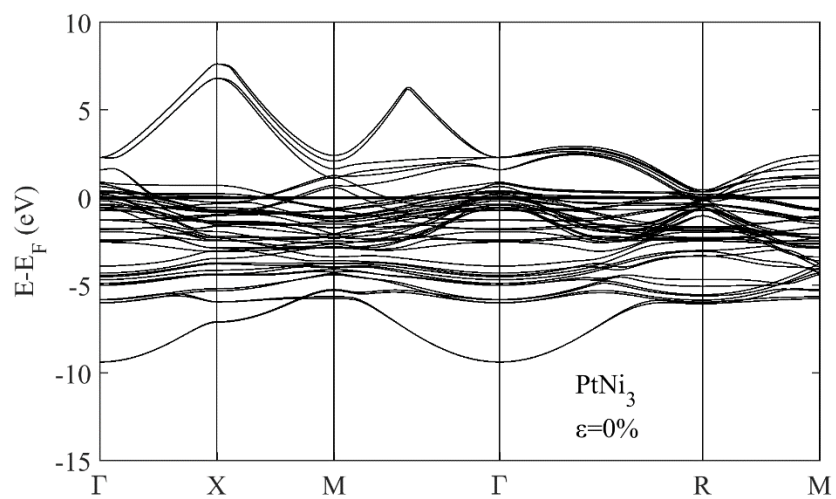
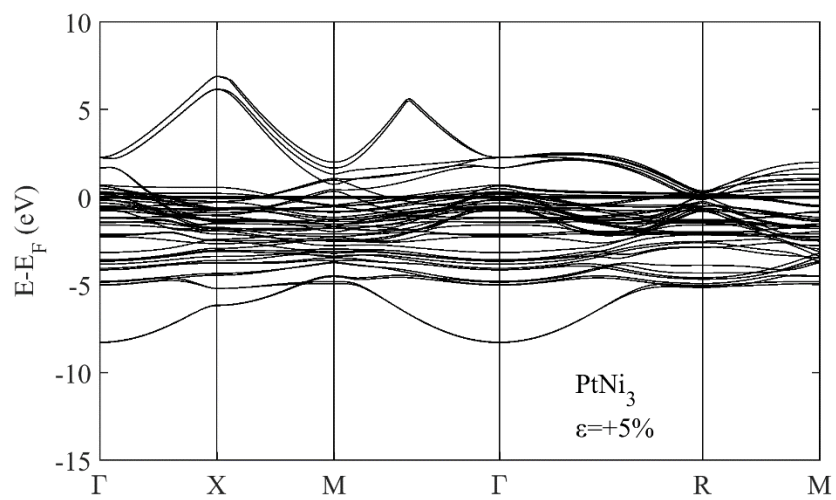


Fig. 5. Stability of  $S_1$ , the expectation value of the  $\sigma_1$  spin operator, under compressive ( $\varepsilon=-5\%$ ) and tensile ( $\varepsilon=+5\%$ ) strain compared to the expectation value under zero ( $\varepsilon=0\%$ ) for the  $\text{Pt}_3\text{Ni}$ ,  $\text{PtNi}$  and  $\text{PtNi}_3$  alloys. The black line has unit gradient; the line of best fit through the data is shown in red and is intended as a guide for the eye.

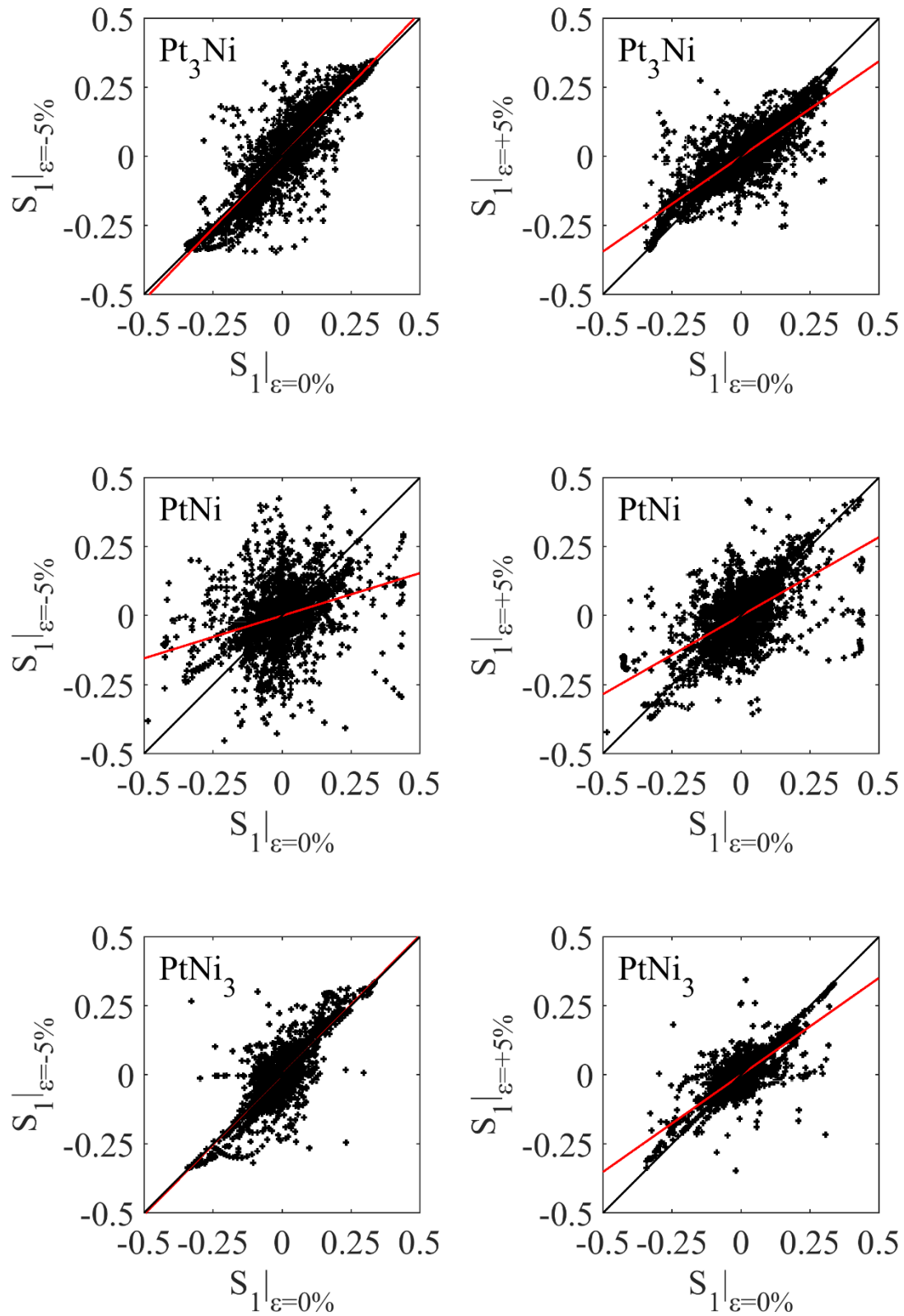


Table S1. Tabulated charge populations for the (a) Pt<sub>3</sub>Ni, (b) PtNi, and (c) PtNi<sub>3</sub> alloys.  $q_{0\%}$  is the occupation of the state when the strain  $\varepsilon = 0\%$  and  $\delta q$  is the change in occupation of the state when then strain  $\varepsilon \neq 0\%$ . C and NC denote collinear and non-collinear simulations, respectively.

(a)

Pt <sub>3</sub> Ni	Pseudopotential semi-core states	$q_{0\%}$ (states)		$\delta q$ (states)		$\delta q$ (states)	
		$\varepsilon = 0\%$		$\varepsilon = +5\%$		$\varepsilon = -5\%$	
		C	NC	C	NC	C	NC
Pt	-	9.9831	9.9831	0.0328	0.0294	-0.0405	-0.0373
	Pt (sp) Ni (sp)	17.8647	17.8454	0.0317	0.0287	-0.0271	-0.0240
	Pt (spf) Ni (sp)	31.8635	31.8445	0.0317	0.0280	-0.0262	-0.0233
Pt s	-	0.4012	0.4011	0.0067	0.0094	-0.0050	-0.0080
	Pt (sp) Ni (sp)	3.0205	3.0248	0.0066	0.0093	-0.0129	-0.0149
	Pt (spf) Ni (sp)	3.0203	3.0244	0.0069	0.0097	-0.0134	-0.0151
Pt p	-	0.8967	0.9314	-0.0035	-0.0053	-0.0184	-0.0150
	Pt (sp) Ni (sp)	5.9979	5.9978	0.0005	0.0005	-0.0008	-0.0008
	Pt (spf) Ni (sp)	5.9979	5.9977	0.0005	0.0006	-0.0008	-0.0008
Pt d	-	8.6852	8.6506	0.0296	0.0253	-0.0170	-0.0144
	Pt (sp) Ni (sp)	8.8464	8.8229	0.0245	0.0187	-0.0135	-0.0083
	Pt (spf) Ni (sp)	8.8456	8.8225	0.0241	0.0178	-0.0121	-0.0073
Ni	-	9.9891	9.9850	-0.0807	-0.0696	0.0939	0.0821
	Pt (sp) Ni (sp)	17.6205	17.6410	-0.0506	-0.0451	0.0607	0.0551
	Pt (spf) Ni (sp)	17.6240	17.6439	-0.0522	-0.0458	0.0606	0.0552
Ni s	-	0.3104	0.3081	-0.0015	0.0005	0.0041	0.0018
	Pt (sp) Ni (sp)	2.8532	2.8578	-0.0057	-0.0023	-0.0007	-0.0031
	Pt (spf) Ni (sp)	2.8533	2.8578	-0.0053	-0.0020	-0.0012	-0.0034
Ni p	-	1.0235	1.0113	-0.0462	-0.0396	0.0405	0.0334
	Pt (sp) Ni (sp)	5.9995	5.9995	0.0001	0.0001	-0.0002	-0.0002
	Pt (spf) Ni (sp)	5.9995	5.9995	0.0001	0.0001	-0.0002	-0.0002
Ni d	-	8.6552	8.6656	-0.0329	-0.0305	0.0494	0.0469
	Pt (sp) Ni (sp)	8.7679	8.7837	-0.0451	-0.0430	0.0615	0.0584
	Pt (spf) Ni (sp)	8.7711	8.7865	-0.0469	-0.0438	0.0621	0.0589

(b)

PtNi	Pseudopotential semi-core states	q <sub>0%</sub> (states)		δq (states)		δq (states)	
		ε = 0%		ε = +5%		ε = -5%	
		C	NC	C	NC	C	NC
Pt	-	9.9656	9.9666	0.0640	0.0585	-0.0828	-0.0698
	Pt (sp) Ni (sp)	17.9396	17.9096	0.0398	0.0389	-0.0548	-0.0563
	Pt (spf) Ni (sp)	31.9385	31.9080	0.0395	0.0391	-0.0561	-0.0558
Pt s	-	0.4071	0.4081	0.0119	0.0135	-0.0093	-0.0116
	Pt (sp) Ni (sp)	3.0487	3.0508	0.0120	0.0142	-0.0186	-0.0195
	Pt (spf) Ni (sp)	3.0485	3.0503	0.0121	0.0144	-0.0188	-0.0196
Pt p	-	0.8785	0.9179	0.0119	0.0073	-0.0232	-0.0170
	Pt (sp) Ni (sp)	5.9971	5.9970	0.0008	0.0008	-0.0010	-0.0010
	Pt (spf) Ni (sp)	5.9971	5.9969	0.0008	0.0008	-0.0010	-0.0010
Pt d	-	8.6800	8.6407	0.0403	0.0376	-0.0503	-0.0413
	Pt (sp) Ni (sp)	8.8937	8.8618	0.0271	0.0239	-0.0352	-0.0358
	Pt (spf) Ni (sp)	8.8931	8.8610	0.0266	0.0238	-0.0363	-0.0352
Ni	-	9.9980	9.9956	-0.0557	-0.0498	0.0711	0.0576
	Pt (sp) Ni (sp)	17.6553	17.6717	-0.0253	-0.0260	0.0507	0.0534
	Pt (spf) Ni (sp)	17.6566	17.6735	-0.0256	-0.0269	0.0527	0.0535
Ni s	-	0.3285	0.3250	0.0021	0.0038	-0.0031	-0.0044
	Pt (sp) Ni (sp)	2.8961	2.8979	0.0055	0.0074	-0.0126	-0.0130
	Pt (spf) Ni (sp)	2.8958	2.8975	0.0057	0.0076	-0.0128	-0.0129
Ni p	-	1.0330	1.0247	-0.0384	-0.0329	0.0258	0.0218
	Pt (sp) Ni (sp)	5.9993	5.9993	0.0002	0.0002	-0.0002	-0.0002
	Pt (spf) Ni (sp)	5.9993	5.9993	0.0002	0.0002	-0.0002	-0.0002
Ni d	-	8.6365	8.6458	-0.0195	-0.0206	0.0485	0.0402
	Pt (sp) Ni (sp)	8.7599	8.7745	-0.0310	-0.0336	0.0635	0.0667
	Pt (spf) Ni (sp)	8.7614	8.7766	-0.0314	-0.0345	0.0658	0.0667

(c)

PtNi <sub>3</sub>	Pseudopotential semi-core states	q <sub>0%</sub> (states)		δq (states)		δq (states)	
		ε = 0%		ε = +5%		ε = -5%	
		C	NC	C	NC	C	NC
Pt	-	9.9329	9.9442	0.0891	0.0785	-0.0927	-0.0841
	Pt (sp) Ni (sp)	18.0136	17.9813	0.0424	0.0435	-0.0556	-0.0537
	Pt (spf) Ni (sp)	32.0118	31.9801	0.0437	0.0431	-0.0541	-0.0543
Pt s	-	0.4121	0.4150	0.0175	0.0183	-0.0153	-0.0160
	Pt (sp) Ni (sp)	3.0866	3.0912	0.0140	0.0159	-0.0204	-0.0219
	Pt (spf) Ni (sp)	3.0864	3.0909	0.0142	0.0159	-0.0205	-0.0219
Pt p	-	0.8633	0.9075	0.0215	0.0147	-0.0267	-0.0177
	Pt (sp) Ni (sp)	5.9963	5.9961	0.0009	0.0010	-0.0013	-0.0013
	Pt (spf) Ni (sp)	5.9962	5.9961	0.0010	0.0010	-0.0012	-0.0013
Pt d	-	8.6574	8.6217	0.0502	0.0455	-0.0506	-0.0504
	Pt (sp) Ni (sp)	8.9307	8.8940	0.0275	0.0266	-0.0338	-0.0306
	Pt (spf) Ni (sp)	8.9294	8.8933	0.0284	0.0261	-0.0323	-0.0310
Ni	-	9.9963	9.9922	-0.0260	-0.0223	0.0252	0.0222
	Pt (sp) Ni (sp)	17.7146	17.7213	-0.0095	-0.0105	0.0207	0.0203
	Pt (spf) Ni (sp)	17.7154	17.7217	-0.0102	-0.0103	0.0205	0.0208
Ni s	-	0.3346	0.3322	0.0069	0.0077	-0.0096	-0.0108
	Pt (sp) Ni (sp)	2.9293	2.9293	0.0079	0.0086	-0.0156	-0.0158
	Pt (spf) Ni (sp)	2.9290	2.9290	0.0081	0.0086	-0.0156	-0.0159
Ni p	-	1.0281	1.0234	0.0286	-0.0260	0.0151	0.0126
	Pt (sp) Ni (sp)	5.9991	5.9991	0.0002	0.0002	-0.0003	-0.0003
	Pt (spf) Ni (sp)	5.9991	5.9991	0.0002	0.0002	-0.0003	-0.0003
Ni d	-	8.6335	8.6367	-0.0042	-0.0042	0.0198	0.0203
	Pt (sp) Ni (sp)	8.7862	8.7929	-0.0176	-0.0193	0.0366	0.0363
	Pt (spf) Ni (sp)	8.7872	8.7936	-0.0185	-0.0192	0.0365	0.0370